Journal of Zhejiang University-SCIENCE A 2025 26(11):1099-1113
www.jzus.zju.edu.cn; www.springer.com/journal/11582
E-mail: jzus_a@zju.edu.cn

Research Article
https://doi.org/10.1631/jzus.A2400539

Design and aerodynamic performance of a wide-speed-range morphing aircraft with horizontal takeoff

Xu ZHANG[1], Binbin YAN[2]✉, Heng ZHANG[3], Yunfei ZHANG[4], Shuangxi LIU[5], Wei HUANG[5]

[1]*Unmanned System Research Institute, Northwestern Polytechnical University, Xi'an 710072, China*
[2]*School of Astronautics, Northwestern Polytechnical University, Xi'an 710072, China*
[3]*School of Aerospace Engineering, Tsinghua University, Beijing 100084, China*
[4]*Shanghai Hangdi Technology Co., Ltd., Shanghai 201818, China*
[5]*Advanced Propulsion Laboratory, National University of Defense Technology, Changsha 410073, China*

Abstract: A wide-speed aircraft capable of horizontal takeoff possesses advantages of rapid response speed, high maneuverability, improved safety, and suitability for different terrains and applications. In this study, a morphing vehicle design with horizontal takeoff and landing capabilities is presented. The aircraft achieves strong aerodynamic performance at subsonic to hypersonic speeds through a wave-like fuselage and a continuously variable sweep angle between 30° and 60°. First, the configuration of the vehicle and its morphing mechanism are described. Then, through numerical modeling, the aerodynamic performance of the vehicle is investigated over a flight profile progressing from horizontal takeoff to hypersonic cruising. These results indicate that different vehicle configurations might be used for different speed ranges so as to optimize performance. The numerical and flow field data also suggest that the effect of the variable sweep angle on the aerodynamic characteristics is weaker in the hypersonic speed range compared to the subsonic range. Overall, the proposed morphing aircraft has excellent aerodynamic characteristics in the speed range of Mach 0.3 to Mach 7. Moreover, its lift coefficients and lift-to-drag ratios in the subsonic phase ensure that horizontal takeoff and landing can be achieved, and its variable sweep angle effectively extends the flight envelope.

Key words: Horizontal takeoff; Morphing aircraft; Variable-sweep-wing; Wide-speed-range vehicle; Aerodynamic characteristics

1 Introduction

Wide-speed-range aircrafts are able to travel at subsonic to hypersonic speeds. Because they fly at higher altitudes and cruise at faster velocities than conventional aircraft, wide-speed vehicles have significant advantages in applications such as transportation and reconnaissance (Feng et al., 2023). Meanwhile, horizontal takeoff and landing can effectively increase safety and reduce flight costs, making aircraft with this ability a focus of cutting-edge aerospace research (Zhao et al., 2018). To maximize the applied value of wide-speed aircraft, it is desired that they be able to fly at altitudes ranging from sea level to near space, and at speeds ranging from subsonic to hypersonic (Zhang et al., 2021). Nevertheless, it is challenging to balance the aerodynamic performance of such vehicles at subsonic and hypersonic speeds, because of the differences in design guidelines for these different conditions. Therefore, a key to improving wide-speed flight lies in optimizing the aerodynamic profile design of the vehicle, based on the harmonization of flying conditions from subsonic to hypersonic speeds (Hu et al., 2016).

Various studies have attempted to address difficulties in aerodynamic layout design for wide-speed vehicles. Some research approached the challenge by employing waverider configuration vehicles. A waverider makes full use of the interaction between the excitation wave and the vehicle, such that the vehicle has a high lift-to-drag ratio at hypersonic speeds, effectively bypassing the lift-to-drag ratio barrier issue (Li et al., 2013). Although waveriders exhibit excellent aerodynamic performance in the hypersonic phase, it is difficult to obtain a waverider configuration with

✉ Binbin YAN, yanbinbin@nwpu.edu.cn
Xu ZHANG, https://orcid.org/0000-0001-7837-7033
Binbin YAN, https://orcid.org/0000-0003-1082-8808

Received Nov. 21, 2024; Revision accepted May 9, 2025;
Crosschecked Oct. 18, 2025

superior aerodynamic performance from subsonic to hypersonic conditions (Li et al., 2014). Thus, to obtain a wide-speed vehicle capable of horizontal takeoff and landing, it is necessary to consider the aerodynamic performance of the vehicle in both the low- and high-speed ranges in an integrated fashion. A fixed-form vehicle could not meet these demands, and so morphing vehicles began to be investigated (Li DC et al., 2018).

Researchers first experimented with morphing mechanisms on aircraft in the subsonic velocity range. Andersen et al. (2007) of NextGen Aeronautics, in collaboration with Piatak from the National Aeronautics and Space Administration (NASA) Langley Research Center, developed and test-flew the MFX-1 aircraft, which has a "sliding skin" wing variant. On the basis of MFX-1, improvements were made to obtain MFX-2, which can achieve a flight altitude of 200 m and a flight speed of 60 m/s (Flanagan et al., 2007). In the same period, Lockheed Martin Aeronautics and Raytheon also proposed a design solution for morphing aircraft, with "folding wings" and "retractable wings" (Bye and McClure, 2007; Ivanco et al., 2007; Love et al., 2007). Ajaj and Jankee (2018) investigated the stability and advantages of asymmetric variable spread-length morphing vehicles. They showed that the design has less drag compared to the conventional approach of aileron deflection and allows for a more agile vehicle. Simultaneously, the control efficiency of the variable spread-length variant is affected by the angle of attack.

Inspired by the biological characteristics of birds and insects, engineers have designed different morphing airfoil forms based on the natural advantages of flying organisms (Li SB et al., 2018). A seagull-like aircraft with a morphing wing utilizing four articulated beams was developed, which displayed increased stability and maneuverability (Abdulrahim and Lind, 2005). The Smartbird is designed with separate inner and outer segments, which allow for more precise shape changes through segmental movements (Mackenzie, 2012; Send et al., 2012). Jitsukawa et al. (2017) designed a new type of foldable wing with feathers at its end. This foldable wing can generate thrust by changing the shape of the feathers, while making the wingspan smaller by folding. Some engineers have also created aircraft inspired by the flight characteristics of bats. Ramezani et al. (2017) developed a bat-like flapping-wing morphing aircraft with pliable and thin airfoils. This bat-like morphing aircraft has flexible deformation capabilities with multiple parts and degrees of freedom, resulting in a strong flight performance (Wang et al., 2024). Khan and Agrawal (2011) designed a flapping-wing mechanism for a micro aircraft based on the shape of an insect called *Allomyrinadi chotoma* and adapted the peak value of the mechanism. Some researchers have also targeted the materials used in morphing structures to improve the performance of aircraft (Battaglia et al., 2024; Riccio et al., 2024). The studies above demonstrate that shape changes can effectively improve the performance of an aircraft, such as its range and cruise time. However, due to the structural characteristics of these morphing structures, the morphing vehicles in the studies above are only suitable for speeds below the speed of sound.

To expand the speed range of aircraft, the application of morphing technology to supersonic vehicles has been investigated. For example, Xie et al. (2024) investigated the flutter mechanism and characteristics of a "diamond-back" folding wing under supersonic inflow using a reduced-order model (ROM)-based aeroelastic method, and Jin et al. (2024) used a parametric design method to study the aero-dynamic characteristics of a deformed wing vehicle with a speed range of Mach 2.5 to Mach 8.5. The United States Naval Laboratory designed a waverider with a fixed leading edge, a fixed upper surface, and a deformable lower surface, which is driven by an actuator. This enables the vehicle to reach a wide range of speeds, between Mach 5 and Mach 10 (Phoenix et al., 2019). Dai et al. (2020) proposed a variable swept-wing waveform configuration based on the delta-wing variable Mach number waveform, which can be deformed to meet the aerodynamic requirements of different missions; the resulting speed of the vehicle ranges from Mach 0.9 to Mach 8. A new morphing mechanism which changes both the plane shape and the profile of the wing was also proposed, and a multi-objective optimization design for this new morphing mechanism was conducted based on the surrogate-based optimization algorithm, in Liu et al. (2022). Luo et al. (2023) adopted a foldable wing configuration to enhance the aerodynamic performance of a hypersonic vehicle, and analyzed the effects of different wing folding angles on the aerodynamic characteristics. Moreover, Chen et al. (2020) investigated the effects of sweep and dihedral angle variations on a wide-speed-range waverider, with results showing that the dihedral angle has a greater effect on the lateral static stability of the vehicle than the sweep angle. Some scholars have also studied guidance and control methods for wide-speed domain variant vehicles based on analysis of their aerodynamic characteristics (Liu et al., 2023; Li X et al., 2024; Zhang et al., 2024a, 2024b).

The main objective of this study is to design an aircraft that has hypersonic cruising velocity and horizontal takeoff and landing capabilities, with improved aerodynamic performance throughout the flight envelope as a result of sweep angle variation. The vehicle's fuselage adopts a wave-rider-like configuration, with a sweep angle that can be switched between three typical angles of 30°, 45°, and 60°. The aerodynamic layout of the vehicle is established through the application of the concepts above, and numerical aerodynamic simulations of sub/trans/super/hypersonic speeds are performed to evaluate the wide-speed-range performance of the design.

The rest of this paper is organized as follows: First, the design concept of the wide-speed-range morphing vehicle and the design parameters are introduced in Section 2. Next, the numerical methods are described in Section 3. Subsequently, the aerodynamic performances of designs with different swept-back angle configurations at varying Mach numbers and altitudes within the flight envelope are compared in Section 4. Preliminary discussions on the differences between configurations are provided in Section 5. Finally, the findings are summarized in Section 6.

2 Design of the horizontal takeoff wide-speed-range morphing aircraft

The proposed aircraft must be able to take off and land horizontally from the runway. To achieve optimal flying performance across a broad range of speeds, the configuration must meet subsonic, transonic, supersonic, and hypersonic flight requirements. According to previous studies on existing wide-speed-range aircraft, the waverider has good lift characteristics at high Mach numbers. However, it is challenging for a hypersonic vehicle with a waverider configuration to meet aerodynamic standards from horizontal takeoff and landing to hypersonic cruising within the entire flight envelope. As a goal of this study, we want the maximum Mach number that the vehicle can achieve to be 7, which is lower than what a traditional waverider can achieve. Thus, in order to improve the performance of the aircraft in the low-speed phase of flight, the front fuselage is designed with a modified waverider configuration.

2.1 General design of the vehicle

The shape of the aircraft was designed with the need for an air inlet (Zhang et al., 2019). Hence, it does not have a smooth upper surface like a pure waverider. In this paper, we only design the aerodynamic profile of the aircraft, and do not specify the design of the air intakes. Compared to a pure waverider, the low-speed performance of the proposed design is superior. However, in order to meet the requirements for horizontal takeoff, the low-speed performance must still be improved. The vehicle's ability to fly at a wide range of speeds is improved by the fused design of the wing, as well as by the waverider-like configuration. Furthermore, the ring volume lift and vortex lift of the wings enable low-speed horizontal takeoff and landing.

To enhance the lift–drag characteristics at varying speeds, a structure with a configurable sweep angle is designed as part of the morphing vehicle. Changes in the sweep angle can be realized by a simple mechanical structure and drive equipment. Using the wing-body transition segment method, the vehicle's body and wings were fused together by the CATIA computer-aided design program. Using this method, the fuselage and wings can be modeled independently, with a defined transition distance between them and a seamless wing profile change achieved through additional transition segments.

The vehicle has a V-tail design, with a sweep drogue of 55°, a tilt of 32°, a drogue chord length of 1.3 m, and a vertical drogue height of about 2.6 m. The rudder is approximately 22% of the vertical height of the tail. The elevator is set at the end of the fuselage in a beavertail configuration. The ailerons are arranged in the outer section of the wing, and the size of the ailerons is mainly affected by the space remaining in the outer section at a 60° sweep angle. The 3-D aerodynamic layout of the vehicle is shown in Fig. 1, and the specific design parameters are shown in Table 1.

2.2 Morphing sweep-back wing design

The proposed vehicle has sweep-back wings with small aspect ratios, and the aerodynamic layout transition is designed using the airfoil transition segment

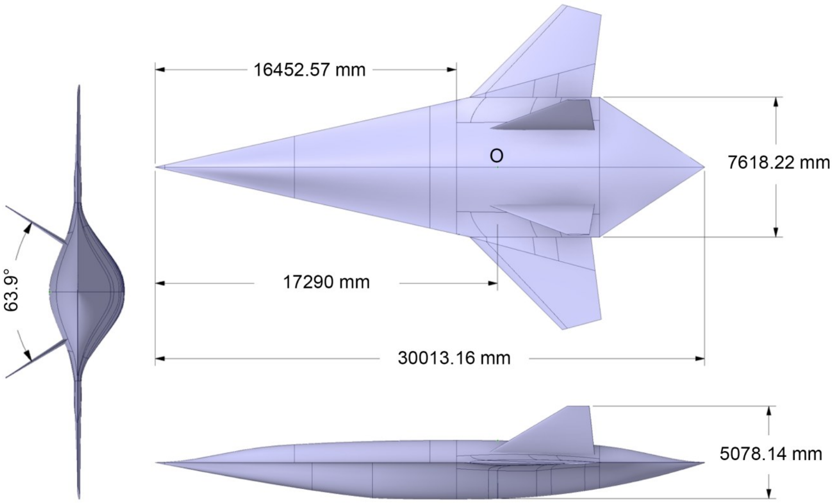

Fig. 1 Three-dimensional view of the vehicle profile

Table 1 Design parameters of the vehicle

Parameter	Value
Length (mm)	30013.16
Width (mm)	17731.26
Height (mm)	5078.14
Wingtip-root ratio	3.12
Leading edge swept-back angle (°)	30, 45, 60
Tail height (m)	2.675
Designed Mach number, *Ma*	0.3–7
Half cone angle of conical flow field (°)	12.5

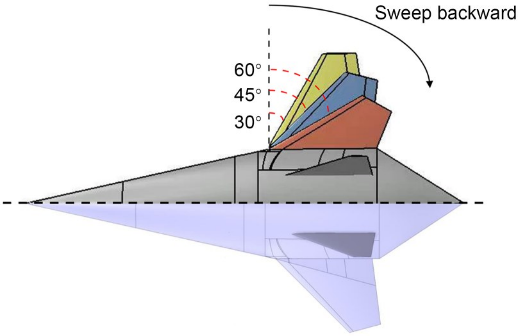

Fig. 2 Change process of the backward sweep angle

method. Smooth profile transitions often mean less drag, which is particularly important for performance in the hypersonic phase. The rotational axis of the variable sweep-back wing is selected at the leading edge of the wing root. The minimum sweep angle is 30°, the maximum sweep angle is 60°, and the intermediate state of the sweep angle is 45°. The aircraft has a maximum wingspan of 20 m at a swept-back angle of 30°. The morphing process of the vehicle's sweep-back wing is shown in Fig. 2, and the vehicle's profile parameters at different sweep angles are presented in Table 2.

A small sweep-back wing configuration has favorable aerodynamic properties at subsonic speeds, allowing the morphing vehicle to take off and land with a wide swept-back wing, which can lower surge drag; this is also beneficial to both supersonic and hypersonic flight. The wings are the primary mechanism for lift generation at low speeds, whereas the fuselage mainly serves as a volume source. The aerodynamic layout of the hypersonic aircraft is primarily based on a waverider-like body, because a conventional layout is insufficient in terms of lift-to-drag ratio for cruising flight at hypersonic speeds. The lift of the vehicle is primarily provided by fuselage compression on the windward side and expansion on the leeward side during cruising. In designing the geometry of the morphing sweep-back wing, the wing profile at a sweep angle of 60° is used as our basis. The basis profile at this sweep angle is then extended to create a folded section, which guarantees the wing profile can be connected to the fuselage at the minimum sweep angle of 30°. A 2° geometric twist was applied to the wingtips in order to enhance the aircraft's leveling performance, and avoid premature stalling of the outer wing segments. Meanwhile, the trailing edge is almost horizontal, which can effectively prevent shape interference during rotation because the trailing edge is relatively far from the rotational axis when the wing rotates around it. As a result, the trailing edge's position changes more significantly during rotation. The primary manifestation

Table 2 Comparison of dimensional parameters at different sweep angles

Sweep angle, Λ (°)	Root chord (m)	Tip chord (m)	Span (m)	Wing area (m^2)	Aspect ratio
30	6.6277	2.2016	20	56.4583	4.83
45	6.6176	2.2016	17.7668	45.0461	4.02
60	7.0895	2.2016	17.7279	33.0080	3.82

of geometric torsion is the sinking of the leading edge of the root wing.

3 Numerical simulation methods

The 3D viscous flow field was simulated using self-developed computational fluid dynamics (CFD) solvers (Miao et al., 2023; Zhang et al., 2023; Li YF et al., 2024), to assess the aerodynamic performance of the wide-speed-range vehicle under various flying situations and sweep angles. In this study, the numerical solution method is based on the Reynolds-averaged Navier Stokes (RANS) equations. This employs a finite-volume method and the k-ω SST (Menter's shear stress transport) turbulence model. The monotonic up wind scheme for conservation laws (MUSCL) is used at Mach 1.5 and below, and the advection up-stream splitting method by pressure-based weight function (AUSMPW+) is utilized from Mach 1.5 up to Mach 7. Time advancement is performed with the implicit lower-upper symmetric Gauss-Seidel relaxation (LU-SGS) method, and the viscosity fluxes are calculated with a second-order central format. An aerospace vehicle model from existing literature is selected to validate the effectiveness and accuracy of the numerical method, and the numerical simulation results are compared to wind tunnel test data (Ding, 2016; Luo et al., 2024). Code validation and grid-independent validation are presented in Section S1 of the electronic supplementary materials (ESM).

4 Aerodynamic characterization analysis

Numerical simulations were performed at various speeds and altitudes to analyze how the aerodynamic properties vary in relation to the sweep angle. With reference to the flight trajectories of SR-71 (Clark et al., 2011), SteamJet (Balepin and Liston, 2001), Manta2025 (Tzong, 2010), and SR-72 (Qu et al., 2025), the calculation points for the simulations were determined as shown in Table 3. The selected subsonic Mach numbers were 0.3 and 0.9, corresponding to altitudes of 0 km and 5 km, respectively. The supersonic Mach numbers of 1.5, 2, and 4 were selected, corresponding to altitudes of 10 km, 14 km, and 16 km, respectively, and hypersonic Mach numbers of 6 and 7 were chosen, corresponding to altitudes of 22 km and 25 km, respectively. The cruising Mach number of the proposed vehicle was set to Mach 7. Under this cruising condition, the static temperature of the atmosphere is 222 K, the static pressure is 2549 Pa, and the dynamic pressure is 874383 Pa. The trajectory of the vehicle was obtained using the Gaussian pseudo-spectral method, so as to verify the validity of the selected envelope.

Table 3 Calculation points of aerodynamic data

Altitude (km)	Temperature (K)	Pressure (Pa)	Mach number, Ma
0	288.150	101325.00	0.3
5	255.676	54048.30	0.9
10	223.252	26499.90	1.5
14	216.650	14170.40	3
16	216.650	10352.80	4
22	218.574	4047.50	6
25	221.552	2549.22	7

4.1 Sub-transonic aerodynamic characterization

The aircrafts with horizontal takeoff capability generally accelerate to Ma=0.8–0.9 after taking off from sea level, followed by an iso-Mach climb to 8–11 km; therefore, the subsonic-state calculation points are chosen as Mach 0.3 and 0.9, corresponding to altitudes of 0 km and 5 km, respectively. In order to accurately analyze the effects of the changes in the angle of attack and sweep angle on the aerodynamic characteristics at subsonic speeds, the change curves of the lift coefficients, drag coefficients, and lift-to-drag ratios for Mach 0.3 and Mach 0.9 vehicles are plotted in Figs. 3 and 4, respectively. In the following text, α, C_{L}, C_{D}, and R_{LD} denote the angle of attack, the lift coefficient, the drag coefficient, and the lift-to-drag ratio, respectively.

From Figs. 3 and 4, it can be seen that C_L rises with α in a roughly linear fashion, while the relationship between the drag coefficient and the angle of attack cannot be described as such. At positive angles of attack, the drag coefficients increase as the attack angles increase, and the drag coefficient at an attack angle of −2° is slightly greater than at an attack angle of 0°. Moreover, as one can observe from Figs. 3 and 4, the drag coefficient C_D increases significantly after the angle of attack exceeds 6°, which is because the induced drag dominates in this condition; furthermore, the frictional drag increases significantly because of the increased separation of the airflow in the wake.

For three typical morphing configurations (sweep angles of 30°, 45°, and 60°), at both Mach 0.3 and Mach 0.9, the optimum lift-to-drag ratios are achieved at α=4°. The optimum lift-to-drag ratio is 8.86 at Mach 0.3, and 9.51 at Mach 0.9. A high lift-to-drag ratio facilitates the vehicle's climbing efficiency in the subsonic phase. It is evident from a comparison of the lift-to-drag ratio statistics that the vehicle's ideal configurations are the configuration at Mach 0.3, and the climbing configuration at Mach 0.9. The improvements in aerodynamic performance for the optimal configuration relative to the other configurations at subsonic speeds are shown in Tables 4 and 5.

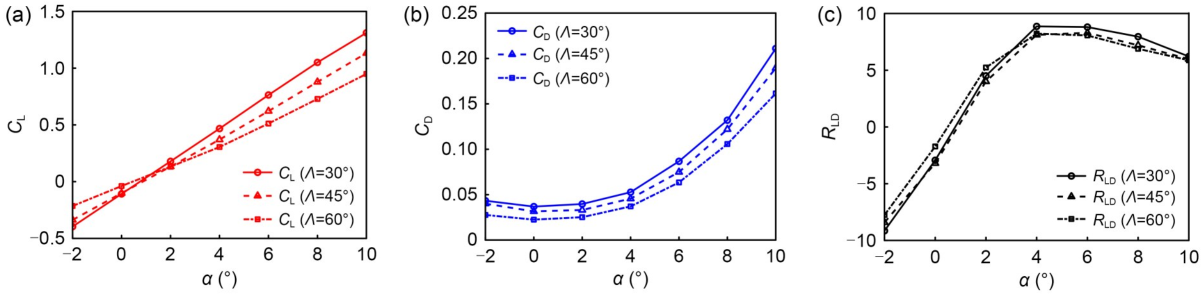

Fig. 3 Aerodynamic parameters in different configurations at Mach 0.3: (a) lift coefficient; (b) drag coefficient; (c) lift-to-drag ratio

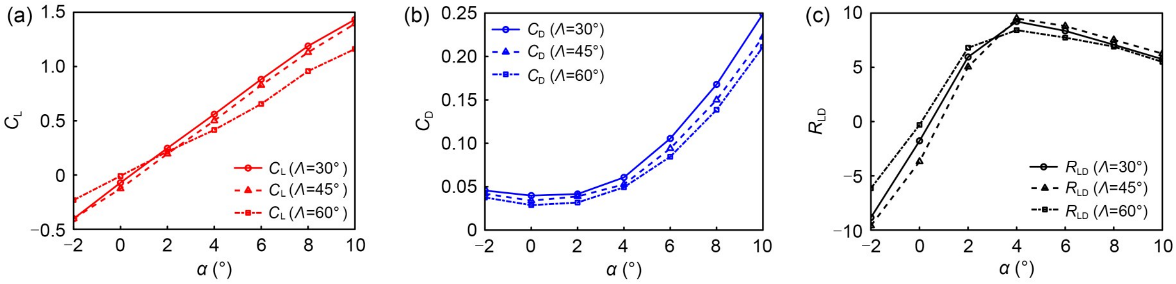

Fig. 4 Aerodynamic parameters in different configurations at Mach 0.9: (a) lift coefficient; (b) drag coefficient; (c) lift-to-drag ratio

Table 4 Aerodynamic performance comparison at Mach 0.3

α	Parameter	Optimal configuration value	Climbing		Cruise	
			Value	Difference (%)	Value	Difference (%)
4°	C_L	0.467490	0.370559	26.158	0.305238	53.156
	R_{LD}	8.864123	8.118865	9.180	8.228413	7.726
6°	C_L	0.763495	0.621466	22.854	0.512310	49.030
	R_{LD}	8.803961	8.297617	6.102	8.067384	9.130
8°	C_L	1.050844	0.878549	19.612	0.728934	44.162
	R_{LD}	7.960348	7.200750	10.549	6.891013	15.518
10°	C_L	1.311340	1.132462	15.796	0.949565	38.099
	R_{LD}	6.214391	5.977370	3.965	5.879365	5.698

4.2 Supersonic aerodynamic characterization

At supersonic speeds, the nature of the flow field in the vicinity of the vehicle changes considerably compared to subsonic speeds. The three Mach numbers selected for investigation in the supersonic range are 1.5, 2, and 4. The resulting calculated aerodynamic parameters are shown in Figs. 5–7, from which it can be seen that the lift-to-drag ratio of the vehicle is maximized when the angle of attack is 6°, and the maximum lift-to-drag ratio is significantly reduced compared to the subsonic data. The main reason for this phenomenon is that in the supersonic phase, the airflow is more effective at suppressing the crossflow, so the

Table 5 Aerodynamic performance comparison at Mach 0.9

α	Parameter	Optimal configuration value	Takeoff		Climbing	
			Value	Difference (%)	Value	Difference (%)
4°	R_{LD}	9.510687	9.227414	3.070	8.432450	12.787
6°	R_{LD}	8.808889	8.361712	5.348	7.741642	13.784
8°	R_{LD}	7.539517	7.083873	6.432	6.910982	9.095
10°	R_{LD}	6.270862	5.755538	8.954	5.505436	13.903

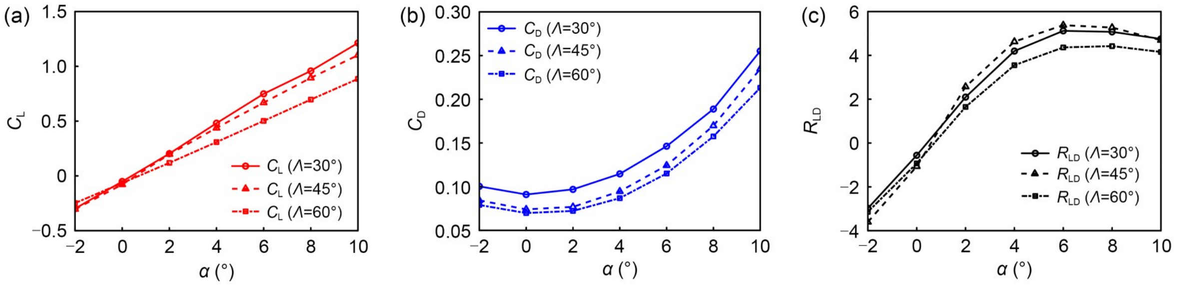

Fig. 5 Aerodynamic parameters in different configurations at Mach 1.5: (a) lift coefficient; (b) drag coefficient; (c) lift-to-drag ratio

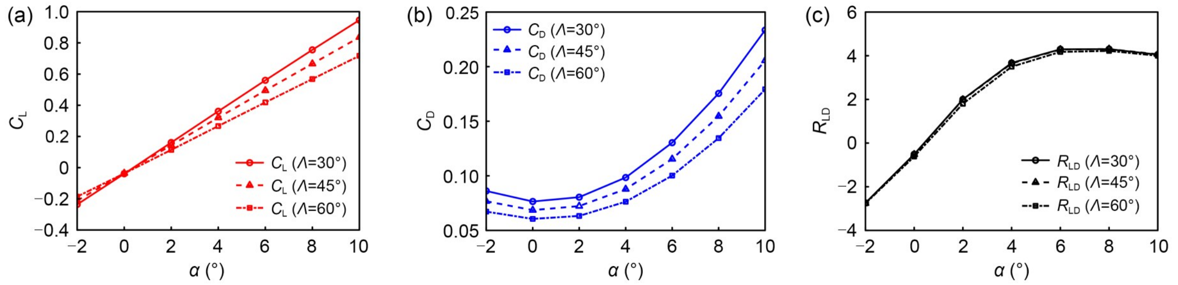

Fig. 6 Aerodynamic parameters in different configurations at Mach 2: (a) lift coefficient; (b) drag coefficient; (c) lift-to-drag ratio

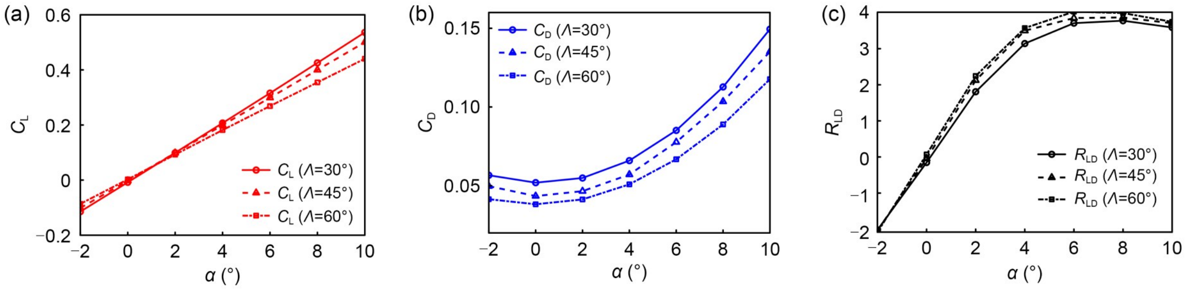

Fig. 7 Aerodynamic parameters in different configurations at Mach 4: (a) lift coefficient; (b) drag coefficient; (c) lift-to-drag ratio

expansion of the vortex is suppressed, and the vortex-driven lift of the aerodynamic layout disappears.

The waverider-like forebody of the morphing vehicle can generate a certain amount of lift under supersonic conditions through the surge effect, thus improving the aerodynamic performance. The maximum lift-to-drag ratios of the vehicle at the three calculation points in the supersonic speed range can all exceed 4. Figs. 4 and 5 show that the climbing configuration has the best lift-to-drag ratio when $\alpha \geqslant 4°$ in the transonic speed range. However, the lift-to-drag ratio is not the only evaluation metric for selecting the optimal configuration. When powered by a turbine-based combined cycle (TBCC) engine, the vehicle is usually selected for level flight or dive acceleration between Mach 0.9 and Mach 1.5, where a lower drag coefficient is desired and the cruise configuration is actually the optimal choice. From further analysis of Figs. 6 and 7, the lift-to-drag ratios of the vehicle are close for the three morphing configurations when the Mach number reaches 2. At Mach 4, the cruise configuration has a significant advantage in terms of lift-to-drag ratio, and becomes the optimal configuration for an altitude-climbing mission. The vehicle begins to approach the hypersonic phase of flight when its speed exceeds Mach 4. At supersonic speeds, the improvements in aerodynamic performance for the optimal configuration relative to the other configurations are shown in Tables 6–8.

4.3 Hypersonic aerodynamic characterization

When the Mach number of the incoming air flow is greater than 5, the vehicle is considered to have entered the hypersonic flight phase. As one can see from Figs. 8 and 9, the slope of the lift coefficient curve for the proposed morphing vehicle decreases with increasing Mach numbers in hypersonic flight, and the non-linearity of the aerodynamic coefficients in the hypersonic section is significantly higher compared to the subsonic and supersonic sections. From the lift-to-drag ratio curves, it can be seen that the vehicle achieves the maximum lift-to-drag ratio at an attack angle of 8° for Mach 6 and Mach 7, which is not consistent with the supersonic conditions.

When considering the climbing requirements, the vehicle should adopt the configuration with the highest lift-to-drag ratio. When entering the cruise phase,

Table 6 Aerodynamic performance comparison at Mach 1.5

α	Parameter	Optimal configuration value	Takeoff		Climbing	
			Value	Difference (%)	Value	Difference (%)
4°	R_{LD}	4.626444	4.196605	10.242	3.551970	30.250
6°	R_{LD}	5.378419	5.119938	5.049	4.363471	23.260
8°	R_{LD}	5.269891	5.073906	3.863	4.423313	19.139
10°	R_{LD}	4.693888	4.751942	−1.221	4.155118	12.966

Table 7 Aerodynamic performance comparison at Mach 2

α	Parameter	Optimal configuration value	Takeoff		Climbing	
			Value	Difference (%)	Value	Difference (%)
4°	R_{LD}	3.648696	3.670153	−0.585	3.496770	4.345
6°	R_{LD}	4.284955	4.294970	−0.233	4.175922	2.611
8°	R_{LD}	4.307270	4.302856	0.103	4.223228	1.990
10°	R_{LD}	4.092902	3.963302	0.327	4.026861	1.640

Table 8 Aerodynamic performance comparison at Mach 4

α	Parameter	Optimal configuration value	Takeoff		Climbing	
			Value	Difference (%)	Value	Difference (%)
4°	R_{LD}	3.572044	3.142008	13.687	3.498019	2.116
6°	R_{LD}	4.024663	3.707456	8.556	3.849338	4.555
8°	R_{LD}	3.987939	3.775135	5.637	3.866089	3.152
10°	R_{LD}	3.743544	3.588487	4.321	3.704026	1.067

the vehicle should adopt the configuration with the lowest drag. In the hypersonic phase, generally speaking, the cruise configuration is the best configuration. The improvements in aerodynamic performance for the optimal configuration relative to the others at hypersonic speeds are shown in Tables 9 and 10. The reasons behind these aerodynamic characteristics will be analyzed in the next section.

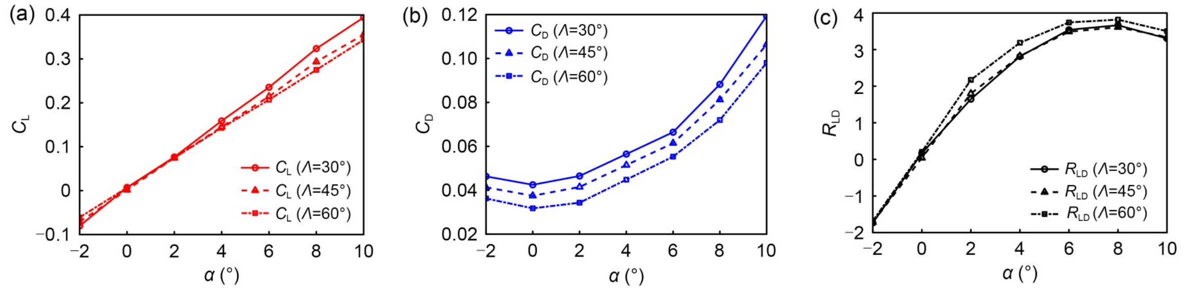

Fig. 8 Aerodynamic parameters in different configurations at Mach 6: (a) lift coefficient; (b) drag coefficient; (c) lift-to-drag ratio

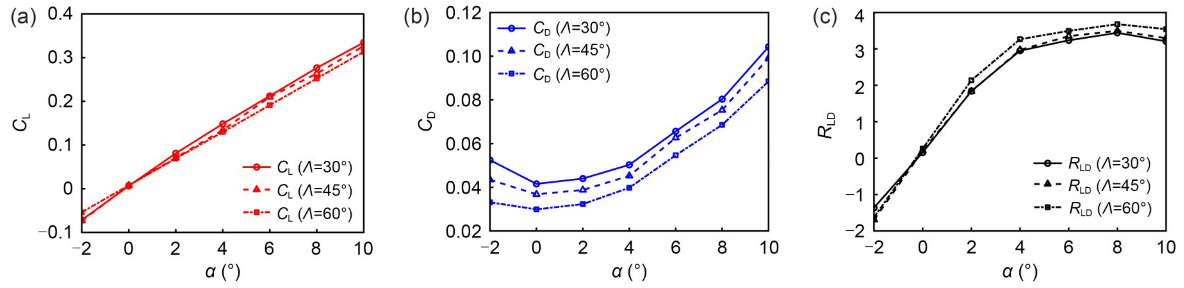

Fig. 9 Aerodynamic parameters in different configurations at Mach 7: (a) lift coefficient; (b) drag coefficient; (c) lift-to-drag ratio

Table 9 Aerodynamic performance comparison at Mach 6

α	Parameter	Optimal configuration value	Takeoff		Climbing	
			Value	Difference (%)	Value	Difference (%)
0°	C_D	0.031748	0.042479	−25.261	0.037479	−15.291
2°	C_D	0.034318	0.046470	−26.151	0.305238	−17.247
2°	R_{LD}	8.864123	8.118865	9.172	8.228413	7.726
4°	R_{LD}	8.864123	8.118865	9.172	8.228413	7.726
6°	R_{LD}	8.803961	8.297617	6.102	8.067384	9.130
8°	R_{LD}	3.819928	3.666365	4.188	3.612421	5.744

Table 10 Aerodynamic performance comparison at Mach 7

α	Parameter	Optimal configuration value	Takeoff		Climbing	
			Value	Difference (%)	Value	Difference (%)
0°	C_D	0.029893	0.041548	−28.052	0.036789	−18.745
2°	C_D	0.032315	0.043981	26.158	0.038781	−16.673
2°	R_{LD}	2.138620	1.844517	15.945	1.800121	16.611
4°	R_{LD}	3.266244	2.951237	10.674	2.823941	9.877
6°	R_{LD}	3.495085	3.235306	8.030	3.541831	4.331
8°	R_{LD}	3.678735	3.441450	6.895	3.496732	5.205

5 Preliminary discussion on configuration differences

In order to analyze the rationale for the differences in aerodynamic performance between different morphing configurations, in this section, we analyze the flow field characteristics under two typical flight conditions (Mach number 0.3, attack angle 0°; Mach number 7, attack angle 6°).

5.1 Analysis of subsonic results

This section focuses on the aerodynamic performance at Mach 0.3 and an attack angle of 0°. In the subsonic phase, the configuration with a 30° sweep angle has the largest lift coefficient, drag coefficient, and lift-to-drag ratio compared to the other two configurations. In addition, the drag coefficients of the three configurations are very similar at attack angles under 2°, but when the attack angle is greater than 6°, their drag coefficients can vary significantly. Fig. 10 shows the distribution of pressure maps on the upper and lower surfaces of the morphing vehicle in different configurations. Specifically, Fig. 10a compares the pressure coefficients on the upper surface of the vehicle for the 30° sweep angle configuration and the 45° sweep angle configuration; Fig. 10c shows a comparison of the pressure coefficients on the lower surface of the vehicle for these two configurations. Fig. 10b compares the pressure coefficients on the upper surface of the vehicle of the 45° sweep angle configuration with the 60° sweep angle configuration; meanwhile, Fig. 10d shows a comparison of the pressure coefficients on the lower surface of the vehicle for these two configurations. All pressure coefficient ratings in Fig. 10 are consistent for the sake of comparison and analysis.

By comparing the pressure coefficients of the vehicle, one can see that the pressure coefficient distribution of the fuselage is essentially the same across different configurations, whereas the pressure cloud map distribution for the wing varies in different configurations. This suggests that the wings of the vehicle have little effect on the fuselage and tail, and the pressure difference between the upper and lower surfaces of the wing is an important source of lift for the vehicle in the subsonic range.

It is clear from Fig. 10 that the upper surface of the wing in the 30° sweep angle configuration has the largest pressure difference, so this is the configuration that can provide the best lift-to-drag ratio at a Mach number of 0.3. Fig. 11 shows the pressure coefficient and streamline distributions of the chord-wise wing profiles for different morphing configurations, where

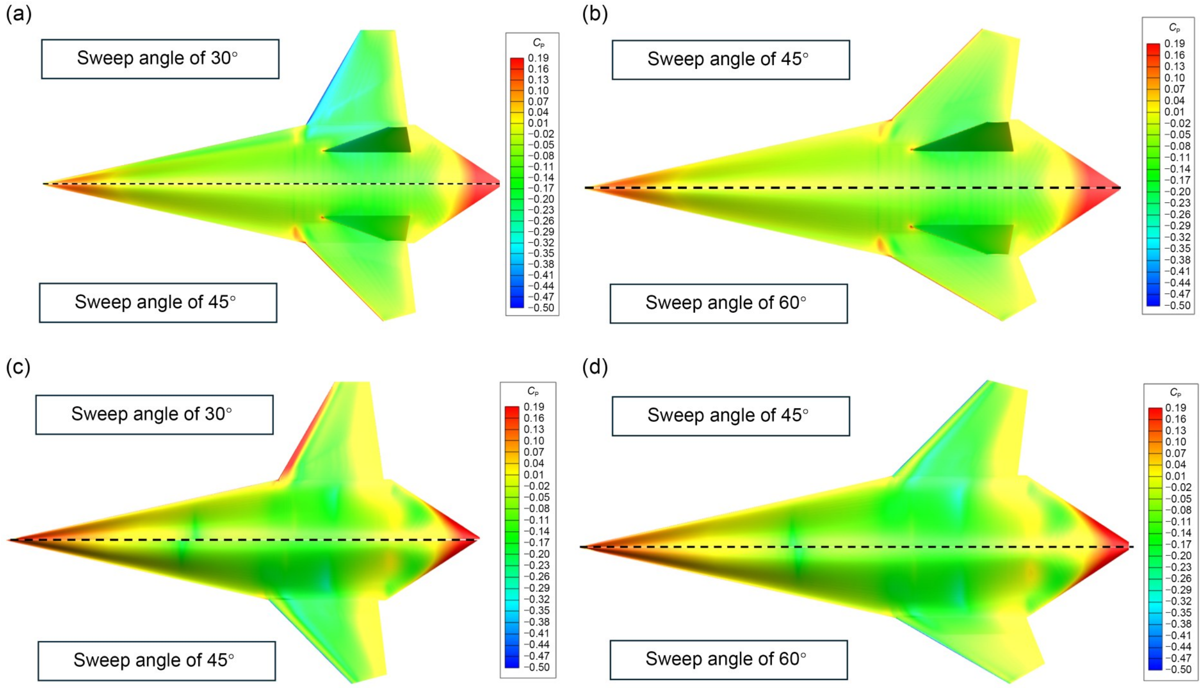

Fig. 10 Comparisons of pressure coefficient (C_p) contours of four configurations (Mach 0.3, α=0°): (a) upper surface (Λ=30° vs. Λ=45°); (b) upper surface (Λ=45° vs. Λ=60°); (c) lower surface (Λ=30° vs. Λ=45°); (d) lower surface (Λ=45° vs. Λ=60°)

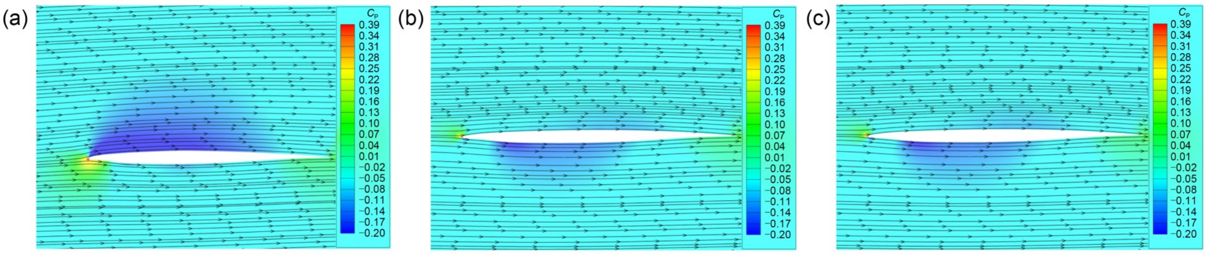

Fig. 11 Pressure coefficient contours on a wing's cross-section in a chord-wise direction (Y=5.6 m) with flow field stream traces (Mach 0.3, α=0°): (a) Λ=30°; (b) Λ=45°; (c) Λ=60°

the position is 5.6 m from the plane of longitudinal symmetry (Y=5.6 m). One can see from Fig. 11 that the maximum low-pressure area is formed above the wing for the 30° sweep angle configuration at Mach 0.3, which is conducive to improving the lift-to-drag ratio of the vehicle. Therefore, the 30° sweep angle is the optimal configuration for sub-transonic speeds, which is in line with the conclusions drawn in Section 4.1.

5.2 Analysis of hypersonic results

Based on the aerodynamic data for the hypersonic-phase vehicle in Section 4.3, it can be seen that the best lift-to-drag ratio is obtained when the attack angle is about 6°. In this section, the pressure distribution at the surface and part of the cross-section of the vehicle is analyzed at Ma=7 and α=6°. It can be observed from Fig. 12 that at Ma=7 and α=6°, the upper and lower surfaces of the vehicle form a substantial pressure difference, which is the main source of the lift obtained by the vehicle. The high-pressure region on the upper surface of the wing is minimized in the 60° sweep angle configuration, which is favorable for improving the aerodynamic performance of the vehicle. To further analyze the pressure distribution between the fuselage cross-section and the wing cross-section, in Figs. 13 and 14, we show the pressure coefficient distributions between the fuselage and the wing for different vehicle profiles at 45° and 60° sweep angle configurations, respectively (X represents the distance from the tip of the aircraft's nose along the fuselage axis to the tail). As one can see, there is a large pressure difference between the upper and lower surfaces of the vehicle fuselage and the wing, which can provide sufficient lift force. However, the difference in pressure distribution between these two configurations is insignificant, indicating that the effect of the variable swept-back wing on the aerodynamic characteristics of the vehicle at high supersonic speeds has been weakened, which is consistent with the variation law of the lift–drag curve.

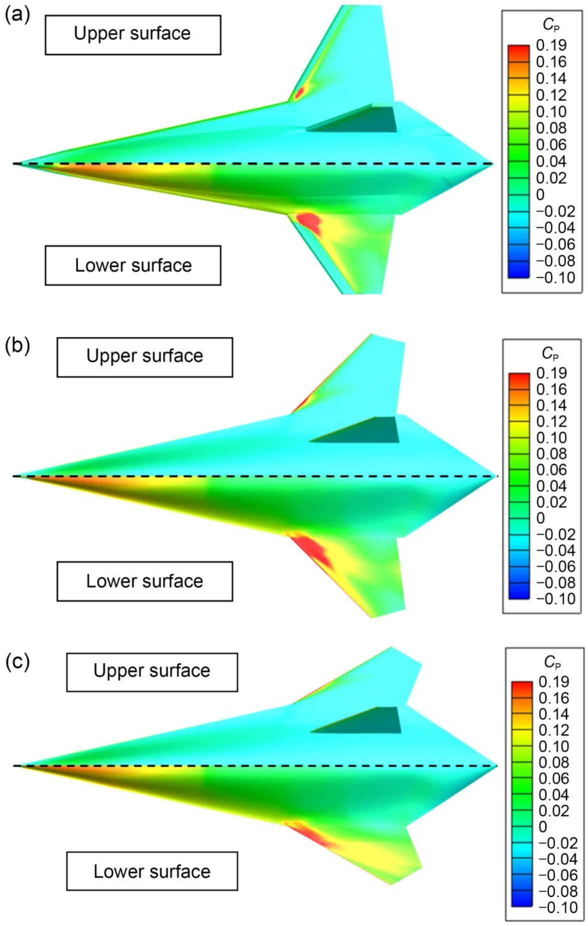

Fig. 12 Comparisons of pressure coefficient contours of the three configurations (Mach 7, α=6°): (a) Λ=30°; (b) Λ=45°; (c) Λ=60°

6 Conclusions

In order to achieve strong aerodynamic performance over subsonic to hypersonic speeds, and to

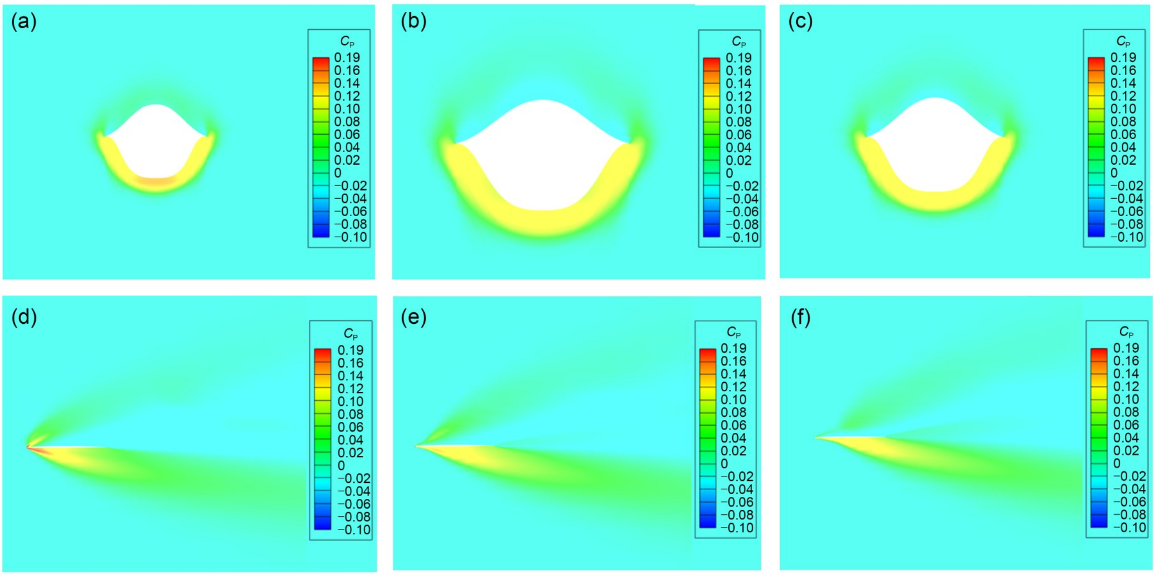

Fig. 13 **Pressure coefficient distributions of fuselage and wing profiles (Λ=45°, Mach 7, α=6°): (a) X=9.6 m; (b) X=7.6 m; (c) X=5.6 m; (d) Y=5.0 m; (e) Y=5.6 m; (f) Y=6.0 m**

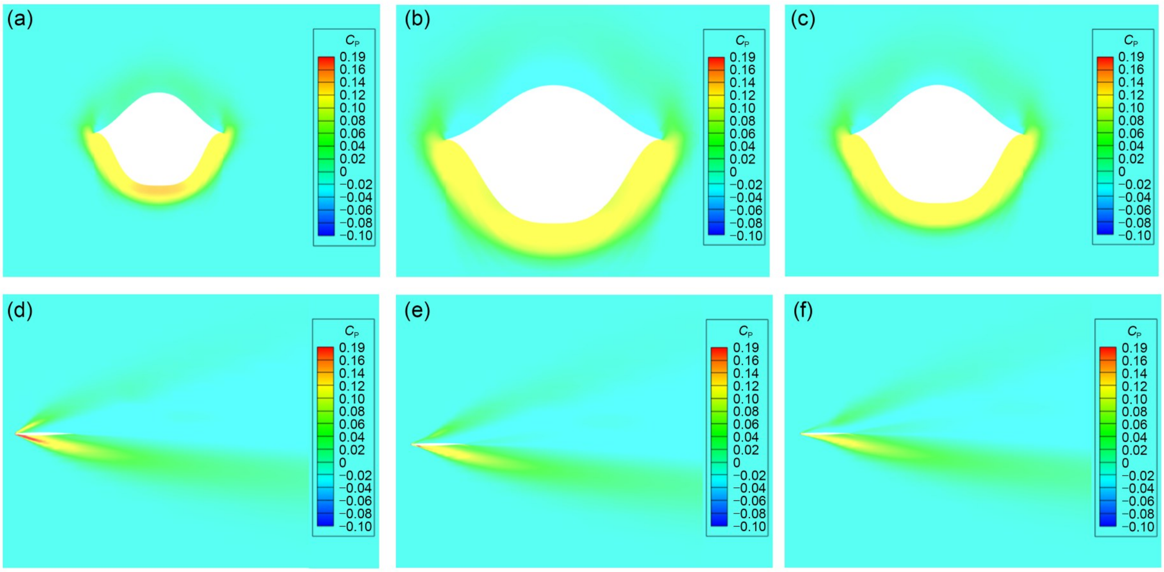

Fig. 14 **Pressure coefficient distributions of fuselage and wing profiles (Λ=60°, Mach 7, α=6°): (a) X=9.6 m; (b) X=7.6 m; (c) X=5.6 m; (d) Y=5.0 m; (e) Y=5.6 m; (f) Y=6.0 m**

enable horizontal takeoff and landing abilities, we propose a novel aircraft design with variable sweep angles. The flow field of this aerodynamic design is analyzed through CFD numerical simulations under the flight conditions of Mach 0.3–7.0 and attack angle −2°−10°, and the aerodynamic performance is compared under three typical morphing configurations: 30°, 45°, and 60° sweep angles.

By analyzing the aerodynamic performance of the vehicle across varying configurations and flight conditions, it is evident that the optimal sweep angles vary with speed. For horizontal takeoff, the most promising of the three typical configurations is the 30° sweep angle. In the transonic to supersonic phases, a 45° sweep angle configuration performs best, while a 60° sweep angle is optimal for the Mach 1.5 to hypersonic phases. These results demonstrate that a morphing-sweep-wing vehicle achieves superior aerodynamic efficiency compared to fixed-wing designs across a broad range of speeds.

By analyzing the aerodynamic data of the aircraft at Mach 0.3, we deduced that a configuration with a 30° sweep angle should be used during the takeoff phase, because of its advantages in terms of lift coefficient and lift-to-drag ratio. The lift-to-drag ratio of the vehicle at this speed reaches a maximum of approximately 8.804, which provides strong aerodynamic support for horizontal takeoff.

Notably, both the lift and drag coefficients of the vehicle decrease with increasing Mach number. The lift coefficient increases with increasing angle of attack, while the drag coefficient also satisfies this law for positive attack angles. Moreover, the lift and drag coefficients of the vehicle differ at varying sweep angles under the same flight conditions. The lift-to-drag ratios under the three different morphing configurations tend to increase and then decrease as the attack angle increases, and the configurations that achieve the optimal lift-to-drag ratio vary depending on the aircraft speed.

In future work, the inlet of the vehicle will be designed based on the optimized aerodynamic profile, and the interactions of airflow through the inlet will be analyzed.

Acknowledgments

This work is supported by the National Natural Science Foundation of China (No. 62173274).

Author contributions

Xu ZHANG designed the research and wrote the first draft of the manuscript. Binbin YAN revised and edited the final version. Heng ZHANG and Yunfei ZHANG conducted the numerical calculation. Shuangxi LIU and Wei HUANG carried out data analysis and verification.

Conflict of interest

Xu ZHANG, Binbin YAN, Heng ZHANG, Yunfei ZHANG, Shuangxi LIU, and Wei HUANG declare that they have no conflict of interest.

References

Abdulrahim M, Lind R, 2005. Control and simulation of a multi-role morphing micro air vehicle. AIAA Guidance, Navigation, and Control Conference and Exhibit. https://doi.org/10.2514/6.2005-6481

Ajaj RM, Jankee GK, 2018. The transformer aircraft: a multi-mission unmanned aerial vehicle capable of symmetric and asymmetric span morphing. *Aerospace Science and Technology*, 76:512-522. https://doi.org/10.1016/j.ast.2018.02.022

Andersen G, Cowan D, Piatak D, 2007. Aeroelastic modeling, analysis and testing of a morphing wing structure. The 48th AIAA/ASME/ASCE/AHS/ASC Structures, Structural Dynamics, and Materials Conference. https://doi.org/10.2514/6.2007-1734

Balepin V, Liston G, 2001. The SteamJet$^{\text{TM}}$: Mach 6+ turbine engine with inlet air conditioning. The 37th Joint Propulsion Conference and Exhibit. https://doi.org/10.2514/6.2001-3238

Battaglia M, Sellitto A, Giamundo A, et al., 2024. Advanced material thermomechanical modelling of shape memory alloys applied to automotive design. *Shape Memory and Superelasticity*, 10(3):297-313. https://doi.org/10.1007/s40830-024-00494-w

Bye D, McClure P, 2007. Design of a morphing vehicle. The 48th AIAA/ASME/ASCE/AHS/ASC Structures, Structural Dynamics, and Materials Conference. https://doi.org/10.2514/6.2007-1728

Chen SH, Liu J, Huang W, et al., 2020. Design methodology of an osculating cone waverider with adjustable sweep and dihedral angles. *Journal of Zhejiang University-SCIENCE A*, 21(9):770-782. https://doi.org/10.1631/jzus.A2000020

Clark C, Kloesel K, Ratnayake N, 2011. A technology pathway for airbreathing, combined-cycle, horizontal space launch through SR-71 based trajectory modeling. 17th AIAA International Space Planes and Hypersonic Systems and Technologies Conference. https://doi.org/10.2514/6.2011-2229

Dai P, Yan BB, Huang W, et al., 2020. Design and aerodynamic performance analysis of a variable-sweep-wing morphing waverider. *Aerospace Science and Technology*, 98:105703. https://doi.org/10.1016/j.ast.2020.105703

Ding F, 2016. Research of a Novel Airframe/Inlet Integrated Full-Waverider Aerodynamic Design Methodology for Air-Breathing Hypersonic Vehicles. PhD Thesis, National University of Defense Technology, Changsha, China (in Chinese).

Feng C, Chen SS, Yuan W, et al., 2023. A wide-speed-range aerodynamic configuration by adopting wave-riding-strake wing. *Acta Astronautica*, 202:442-452. https://doi.org/10.1016/j.actaastro.2022.11.010

Flanagan J, Strutzenberg R, Myers R, et al., 2007. Development and flight testing of a morphing aircraft, the NextGen MFX-1. The 48th AIAA/ASME/ASCE/AHS/ASC Structures, Structural Dynamics, and Materials Conference. https://doi.org/10.2514/6.2007-1707

Hu XZ, Chen XQ, Parks GT, et al., 2016. Review of improved Monte Carlo methods in uncertainty-based design optimization for aerospace vehicles. *Progress in Aerospace Sciences*, 86:20-27. https://doi.org/10.1016/j.paerosci.2016.07.004

Ivanco T, Scott R, Love M, et al., 2007. Validation of the Lockheed Martin morphing concept with wind tunnel testing. The 48th AIAA/ASME/ASCE/AHS/ASC Structures, Structural Dynamics, and Materials Conference.

https://doi.org/10.2514/6.2007-2235

Jin ZK, Yu ZH, Meng FS, et al., 2024. Parametric design method and lift/drag characteristics analysis for a wide-range, wing-morphing glide vehicle. *Aerospace*, 11(4):257. https://doi.org/10.3390/aerospace11040257

Jitsukawa T, Adachi H, Abe T, et al., 2017. Bio-inspired wing-folding mechanism of micro air vehicle (MAV). *Artificial Life and Robotics*, 22(2):203-208. https://doi.org/10.1007/s10015-016-0339-9

Khan ZA, Agrawal SK, 2011. Study of biologically inspired flapping mechanism for micro air vehicles. *AIAA Journal*, 49(7):1354-1365. https://doi.org/10.2514/1.J050447

Li DC, Zhao SW, da Ronch A, et al., 2018. A review of modelling and analysis of morphing wings. *Progress in Aerospace Sciences*, 100:46-62. https://doi.org/10.1016/j.paerosci.2018.06.002

Li SB, Luo SB, Huang W, et al., 2013. Influence of the connection section on the aerodynamic performance of the tandem waverider in a wide-speed range. *Aerospace Science and Technology*, 30(1):50-65. https://doi.org/10.1016/j.ast.2013.07.003

Li SB, Huang W, Wang ZG, et al., 2014. Design and aerodynamic investigation of a parallel vehicle on a wide-speed range. *Science China Information Sciences*, 57(12):1-10. https://doi.org/10.1007/s11432-014-5225-2

Li SB, Wang ZG, Huang W, et al., 2018. Design and investigation on variable Mach number waverider for a wide-speed range. *Aerospace Science and Technology*, 76:291-302. https://doi.org/10.1016/j.ast.2018.01.044

Li X, Wang XG, Zhou HY, et al., 2024. A novel evasion guidance for hypersonic morphing vehicle via intelligent maneuver strategy. *Chinese Journal of Aeronautics*, 37(5):441-461. https://doi.org/10.1016/j.cja.2024.02.024

Li YF, Xiang YY, Shi LJ, et al., 2024. Efficient reliability analysis via a nonlinear autoregressive multi-fidelity surrogate model and active learning. *Journal of Zhejiang University-SCIENCE A*, 25(11):922-937. https://doi.org/10.1631/jzus.A2300340

Liu B, Liang H, Han ZH, et al., 2022. Surrogate-based aerodynamic shape optimization of a morphing wing considering a wide Mach-number range. *Aerospace Science and Technology*, 124:107557. https://doi.org/10.1016/j.ast.2022.107557

Liu SX, Yan BB, Huang W, et al., 2023. Current status and prospects of terminal guidance laws for intercepting hypersonic vehicles in near space: a review. *Journal of Zhejiang University-SCIENCE A*, 24(5):387-403. https://doi.org/10.1631/jzus.A2200423

Love M, Zink P, Stroud R, et al., 2007. Demonstration of morphing technology through ground and wind tunnel tests. The 48th AIAA/ASME/ASCE/AHS/ASC Structures, Structural Dynamics, and Materials Conference. https://doi.org/10.2514/6.2007-1729

Luo SB, Yue H, Liu J, 2023. Optimization design of aerodynamic layout for hypersonic morphing aircraft. *Electronic Technology & Software Engineering*, (2):51-55 (in Chinese). https://doi.org/10.20109/j.cnki.etse.2023.02.013

Luo SB, Yue H, Liu J, et al., 2024. Study on aerodynamic performance of morphing hypersonic vehicle in wide-speed range. *Transactions of Nanjing University of Aeronautics and Astronautics*, 41(2):184-201. https://doi.org/10.16356/j.1005-1120.2024.02.005

Mackenzie D, 2012. A flapping of wings. *Science*, 335(6075): 1430-1433. https://doi.org/10.1126/science.335.6075.1430

Miao XJ, Gao GJ, Wang JB, et al., 2023. Effect of low operating temperature on the aerodynamic characteristics of a high-speed train. *Journal of Zhejiang University-SCIENCE A*, 24(3):284-298. https://doi.org/10.1631/jzus.A2200166

Phoenix AA, Rogers RE, Maxwell JR, et al., 2019. Mach five to ten morphing waverider: control point study. *Journal of Aircraft*, 56(2):493-504. https://doi.org/10.2514/1.C034901

Qu F, Wang Q, Cheng SW, et al., 2025. Aerodynamic shape optimization design of airframe/propulsion integrated hypersonic aircraft with aerodynamics/trajectory/control coupling. *Acta Aeronautica et Astronautica Sinica*, 46(4): 130874 (in Chinese). https://doi.org/10.7527/S1000-6893.2024.30874

Ramezani A, Chung SJ, Hutchinson S, 2017. A biomimetic robotic platform to study flight specializations of bats. *Science Robotics*, 2(3):aal2505. https://doi.org/10.1126/scirobotics.aal2505

Riccio A, Sellitto A, Battaglia M, 2024. Morphing spoiler for adaptive aerodynamics by shape memory alloys. *Actuators*, 13(9):330. https://doi.org/10.3390/act13090330

Send W, Fischer M, Jebens K, et al., 2012. Artificial hinged-wing bird with active torsion and partially linear kinematics. The 28th International Congress of the Aeronautical Sciences, p.1-10.

Tzong G, Jacobs R, Liguore S, 2010. Air Vehicle Integration and Technology Research (AVIATR) Task Order 0015: Predictive Capability for Hypersonic Structural Response and Life Prediction: Phase 1-Identification of Knowledge Gaps. The Boeing Company, USA.

Wang F, Pei XB, Wu GX, et al., 2024. Analysis and design of bat-like flapping-wing aircraft. *Aerospace*, 11(4):325. https://doi.org/10.3390/aerospace11040325

Xie PZ, Ye K, Xie PT, et al., 2024. Supersonic flutter mechanism of "diamond-back" folding wings. *Aerospace Science and Technology*, 153:109396. https://doi.org/10.1016/j.ast.2024.109396

Zhang H, Li J, Yang Z, 2023. Double-decoupled inverse design of natural laminar flow nacelle under transonic conditions. *Chinese Journal of Aeronautics*, 36(6):1-18. https://doi.org/10.1016/j.cja.2023.04.016

Zhang H, Wang P, Tang GJ, et al., 2024a. Fixed-time attitude control for hypersonic morphing vehicles: a dynamic memory event-triggering approach. *Aerospace Science and*

Technology, 155:109577.
https://doi.org/10.1016/j.ast.2024.109577

Zhang H, Wang P, Tang GJ, et al., 2024b. Fuzzy disturbance observer-based fixed-time attitude control for hypersonic morphing vehicles. *IEEE Transactions on Aerospace and Electronic Systems*, 60(5):6577-6593.
https://doi.org/10.1109/TAES.2024.3404911

Zhang TT, Yan XT, Huang W, et al., 2021. Multidisciplinary design optimization of a wide speed range vehicle with waveride airframe and RBCC engine. *Energy*, 235:121386.
https://doi.org/10.1016/j.energy.2021.121386

Zhang WH, Liu J, Ding F, et al., 2019. Novel integration methodology for an inward turning waverider forebody/inlet. *Journal of Zhejiang University-SCIENCE A*, 20(12):918-926.
https://doi.org/10.1631/jzus.A1900334

Zhao ZT, Huang W, Yan BB, et al., 2018. Design and high speed aerodynamic performance analysis of vortex lift waverider with a wide-speed range. *Acta Astronautica*, 151:848-863.
https://doi.org/10.1016/j.actaastro.2018.07.034

Electronic supplementary materials

Section S1